Measuring carbon dioxide emissions from liquefied natural gas (LNG) terminals with imaging spectroscopy

Zhan Zhang[1], Daniel H. Cusworth[2,3], Alana K. Ayasse[2,3], Evan D. Sherwin[1], Adam R. Brandt[1]

[1]Department of Energy Science & Engineering, Stanford University, Stanford, California 94305, United States
[2]Arizona Institutes for Resilience, University of Arizona, Tucson, AZ, United States
[3]Carbon Mapper, 12 S Raymond Ave, Pasadena, California 91105, United States

Key Points:

- 22 CO_2 emission events from Sabine Pass and Cameron LNG terminals are found and quantified by airborne imaging spectrometers
- Imaging spectrometers are capable of measuring power plant CO_2 emissions with relatively high agreement with *in situ* measured data
- Compared to power plant, LNG terminal CO_2 plumes are smaller in spatial extent, with lower emission rates and more background noise

Corresponding author: Zhan Zhang, `zz221636@stanford.edu`

Abstract

The rapid growth of liquefied natural gas (LNG) exports underscores the importance of CO_2 monitoring for LNG export terminals. This study presents a method for measuring CO_2 emissions using remote sensing imaging spectroscopy applied to LNG terminals. The method is first validated using 47 power plant emission events with *in situ* measured data, then applied to 22 emission events in Sabine Pass and Cameron LNG terminals. The power plant dataset shows a robust correlation between our emission rate estimates and *in situ* data, with R^2 0.9146 and the average error -2%. At Sabine Pass, 8 point sources are identified with emission rates ranging from 219.69 ± 54.95 to 1083.22 ± 308.06 t/hr. At Cameron, 3 point sources are identified with emission rates ranging from 91.64 $\pm$ 25.81 to 265.61 ± 67.80 t/hr. This study illustrates the potential of remote sensing to validate environmental reporting and CO_2 inventories for industrial facilities.

Plain Language Summary

The natural gas system is an important source of carbon dioxide (CO_2) emissions. Rising domestic production of natural gas in the U.S. and the international energy demand have contributed to a rapid growth of liquefied natural gas (LNG) exports. This makes it increasingly important to assess the CO_2 emissions along the LNG supply chain, especially during gas liquefaction at LNG export terminals. However, existing inventories only provide annual/monthly emissions data reported by LNG operators for some major LNG terminals, and those data lack measurement-based *in situ* validation. Here we introduce a top-down CO_2 measuring method using remote sensing imaging spectroscopy, which is able to provide an independent third-party CO_2 emissions data source with uniform measuring technology across all infrastructure. Additionally, the emission measurements obtained by this method would help enable rapid responses to any unexpected increases in emissions. When combined with remote sensing methane detection, this technology can further contribute to a more efficient monitoring system of the carbon emissions along the natural gas supply chain. This study also shows the mapping and quantification capability of imaging spectroscopy on the plumes with emission rate of 100-3000 t CO_2/hr, implying its potential for broader applications in CO_2 top-down detection.

1 Introduction

Natural gas (NG) accounts for 22% of global fossil carbon dioxide (CO_2) emissions, following coal (41%) and oil (32%) in 2021 (Friedlingstein et al., 2022). To reduce greenhouse gas (GHG) emissions from the NG system, it is crucial to quantify and understand how emissions are distributed throughout the NG supply chain (Hamedi et al., 2009; Zarei & Amin-Naseri, 2019).

The liquefied natural gas (LNG) supply chain is a special component in the broader NG supply chain. It is commonly used for long-distance transportation by sea. The United States plays an important role in the international LNG market. With the shale gas revolution boosting domestic production from 2016, it rapidly emerged as the world's leading LNG exporter (U.S. EIA, 2022). In 2022, U.S. LNG exports reached 10.6 billion cubic feet per day (Bcf/d), tying Qartar as the world's top LNG exporter (U.S. EIA, 2023). The rapid growth of U.S. LNG exports underscores the growing importance of assessing GHG emissions in the U.S. LNG supply chain and developing methods that can be applied internationally.

In addition to the upstream stages and downstream combustion stage, in which NG is generally in gaseous form, the LNG supply chain comprises three stages: liquefaction, transportation and regasification (Balcombe et al., 2017). Typically, NG is converted into its liquefied state at liquefaction trains, then transported via special ocean-going LNG

carriers, and finally reconverted to its gaseous state at regasification terminals. As of 2022, U.S. has a total of seven industrial-scale LNG export terminals, with total liquefaction capacity of over 92 million tonnes per annum (mtpa) (Alam et al., 2023), most of which are located in the United States Gulf Coast states of Louisiana and Texas (Table S1).

Previous studies show that liquefaction accounts for the highest proportion of GHG emissions across the three-stage LNG supply chain. These emissions are mainly from fuel combustion for refrigeration compressors and generator turbines. A small amount is also from flare combustion to destroy waste gases. Abrahams et al. (2015) collected lique-faction emissions estimates from various studies and reported a range of 2.4-8.8 g CO_2 eq/MJ, compared to the end-use combustion emissions of 43-50 g CO_2 eq/MJ for final gas combustion in electricity generation. Balcombe et al. (2017) and Gan et al. (2020) concluded similar ranges of 4.1-7.7 g CO_2 eq/MJ and 4.1-7.6 g CO_2 eq/MJ from liter-ature search and environment assessment reports, respectively. However, the data in the past studies are mostly from LNG operators or past literature, which are often not trans-parent in their measuring technology. Some studies calculated liquefaction emissions by collecting emission factors and activity factors (Cohen, 2013; Barnett, 2010; Okamura et al., 2007). But most of these data are before the U.S. shale gas production surge (U.S. EIA, 2022), thus become less valuable in the current LNG industry. And practical ex-perience in methane emissions estimation suggests that calculated emissions can differ greatly from empirical measurements of emissions for the same facility or region (Chen et al., 2022; E. Sherwin et al., 2023)

Given the substantial increase of U.S. LNG exports and the importance of CO_2 emis-sions in the liquefaction stage, the development of a monitoring system for liquefaction CO_2 emissions at LNG export terminals is of growing importance. The Greenhouse Gas Reporting Program (GHGRP) operated by the U.S. Environmental Protection Agency (U.S. EPA) produces the valuable Facility Level Information on GreenHouse gases Tool (FLIGHT) dataset (U.S. EPA, 2022). FLIGHT includes annual and monthly CO_2 emis-sions data for five out of the seven major LNG terminals (excluding Calcasieu Pass and Elba Island), based on estimates reported by LNG operators at the total facility level and at the equipment/unit level. However, there is currently not an independent third-party source for emissions measurement data at LNG terminals using uniform measur-ing technology across all infrastructure. It would also be valuable to complement FLIGHT data with more frequent emission measurements, enabling rapid response to any unex-pected increases in emissions.

Remote sensing imaging spectroscopy could enable more rapid, independent mon-itoring of LNG terminal CO_2 emissions. These instruments measure the solar radiance reflected off the Earth's surface at many wavelengths, providing insight into surface and atmospheric properties (Cusworth et al., 2021). The Next-Generation Airborne Visible/Infrared Imaging Spectrometer (AVIRIS-NG) and the Global Airborne Observatory (GAO) have been proven effective for methane emissions measuring because of their fine spatial res-olution (2-10 m) and spectral resolution (5 nm sampling between 400-2500 nm) (Duren et al., 2019; Frankenberg et al., 2016; Asner et al., 2012). Because these spectrometers also cover the shortwave infrared wavelength range, where atmospheric CO_2 strongly ab-sorbs solar radiance, they can also be leveraged for CO_2 measuring. Dennison et al. (2013) and Thorpe et al. (2017) did CO_2 mapping on power plants using AVIRIS and AVIRIS-NG, confirming the capability of imaging spectrometers for CO_2 detection. Cusworth et al. (2021) conducted the first facility-scale CO_2 emissions quantification study using data from AVIRIS-NG, GAO, and the satellite spectrometer PRISMA. By employing the Iterative Maximum A Posteriori–Differential Optical Absorption Spectroscopy (IMAP-DOAS) method, they estimated emissions from 17 coal and gas fired power plants in the U.S., with robust correlation and 21% average estimate error with simultaneous *in situ* measured data. Foote et al. (2021) also quantified 7 CO_2 emissions examples, conclud-ing that generating the scene-specific unit enhancement spectra could achieve quantifi-

cation improvement. However, it is important to note that these studies have primarily focused on power plants, as they are often high-volume point sources of CO_2 emissions equipped with continuous emissions monitoring systems (CEMS) that provide *in situ* measured data for calibration purposes (U.S. EPA, 2023). Until now, there is still a lack of studies on the measuring of smaller-volume CO_2 emissions from other sources, such as LNG terminals.

In this study, we present an updated matched filter method of CO_2 emissions measuring, which is different from the method in Cusworth et al. (2021), and apply it to LNG terminals using imaging spectroscopy data from AVIRIS-NG and GAO. The method is first validated by 47 power plant emission events with *in situ* measured data. Subsequently, the calibrated method is applied to 22 emission events in two major LNG terminals: Sabine Pass and Cameron. Based on these measurements, an estimation of the life-cycle carbon intensity (CI) of the liquefaction process is also conducted. Compared to existing LNG terminal CO_2 emissions data which largely rely on LNG operators, this method provides an independent third-party data source with uniform measuring technology. It could also be used in regions or industries without rigorous emissions reporting. Additionally, the emission measurements obtained by this method would help enable rapid responses to any unexpected increases in emissions. If with more emission samples, our method is going to be able to provide a more robust life-cycle CI estimation for the LNG liquefaction process. When combined with methane detection, it can further contribute to a more efficient monitoring system of the carbon emissions along the LNG supply chain. This study also shows the mapping and quantification capability of imaging spectroscopy on power plant CO_2 emissions, implying its potential for broader applications in CO_2 top-down detection.

2 Methods

In this study, two datasets from AVIRIS-NG and GAO imagery are collected, focusing on coal/natural gas-fired power plants and LNG terminals, respectively. The power plant dataset comprises 47 emission events from 22 facilities in 2017-2022. Among these infrastructure, 13 are coal-fired power plants, and 9 are gas-fired. For the ground-truths at power plants, we rely on hourly *in situ* measured CO_2 volumes of these power plants from CEMS data (U.S. EPA, 2023). The LNG terminal dataset consists of 22 emission events in two major terminals: Sabine Pass and Cameron, all in 2021-2022. These LNG terminals do not report *in situ* CEMS data. Specific steps of detection and quantification are as follows.

2.1 Detection

The CO_2 retrieval method in this study is adapted from the matched filter methane retrieval method in Thorpe et al. (2016). It uses a sparse matched filter with albedo correction to retrieve gas concentration-pathlength enhancements from the calibrated and orthorectified radiance from raw imagery. The resulting concentration-pathlength enhancement, also known as the mixing ratio length (α), is measured in parts per million meter (ppm-m), where *ppm* represents concentration and m represents the path length over which absorption occurs. This methane retrieval method has been demonstrated to be capable of detecting plumes with emissions as small as 2-10 kg CH_4/hr (Thorpe et al., 2016; Duren et al., 2019). Compared to CH_4 retrieval, the CO_2 retrieval method makes several key adjustments. First, it uses wavelength bands within the range 1928-2200 nm where CO_2 has strong absorption effects on the radiance. Second, it simulates CO_2 concentration enhancements above background, starting at 0 ppm-m and incrementally doubling up from 20,000 ppm-m to 1,280,000 ppm-m (Foote et al., 2021). Finally, it applies an independent matched filter to a group of 50 adjacent columns of the im-

age to improve the covariance estimate by suppressing artifacts from non-uniformity among detector elements (Ayasse et al., 2019).

The resulting CO_2 enhancement imagery is then analyzed manually to identify the presence of a CO_2 plume. During this step, a Red, Green, Blue (RGB) image is generated from raw radiance data, and hourly wind data of this area are collected from the Dark Sky API (Apple Inc., 2023) to assist identification (see details in Section S1).

In addition, to improve the accuracy of quantification, we conduct an automatic artifact masking process to remove certain artifacts close to the CO_2 plume. One such artifact occurs when the plume source is in close proximity to a roof painted with white paint. This can result in short-wave infrared (SWIR) absorption due to hydrocarbon absorption from oil-based paints (Ayasse et al., 2018). Another example is the presence of flaring, which can lead to sensor saturation in the SWIR bands while emitting CO_2. Note that excluding these pixels from quantification may introduce low bias if it does not change the plume length (see details in Section S2).

2.2 Quantification

After detection, the next step is quantifying the emission rate of the identified CO_2 plume. We first define a circular area around the plume, centered on the plume origin, with a radius called the fetch radius (r_c). The circle reaches the plume boundary to ensure complete coverage (i.e., r_c approximates the plume length, further details described in Section 2.3). Within the area, we define a minimum (α_l) and a maximum (α_h) threshold for the mixing ratio length α, so that the pixels out of the range α_l-α_h would be excluded from quantification. We also define a merge distance, which allows for a definition of contiguous plumes in the presence of gaps inside the circle. Therefore, the pixels within the range $\alpha_l - \alpha_h$ and with distance less than or equal to the merge distance are included into quantification (see details in Section S3).

Next, we calculate the integrated mass enhancement (IME) of the plume within the circle as follows:

$$IME_{r_c} = k \sum_{i=0}^{n} \alpha(i)S(i)$$ (1)

Where $i \in [0, N]$ are the pixels of the plume, α is the mixing ratio length of each pixel, S is the pixel area, and the constant k represents the conversion factor from concentration-pathlength to mass. Here we calculate the ratio of IME/r for each radius from the initial radius (pixel size) to the fetch radius, increasing by the pixel size ($r = r_1, r_2, \ldots, r_j, \ldots, r_c$). Then the average of the IME/r estimates $\overline{IME}/r$ and the 10-meter wind speed from Dark Sky API (Apple Inc., 2023) are used to calculate the emission rate:

$$Q = (\overline{IME}/r)U_{10}$$ (2)

Note that this method includes all the valid pixels within the circle identified as containing a CO_2 enhancement without attempting to separate a masked plume. Therefore, this approach may include small background noise enhancements into the estimated overall mass enhancement (see Section 3.1).

2.3 Fetch Radius Calculation

The fetch radius r_c is an important input during quantification as shown in equation 1 and 2. However, manual determination of r_c can be time-consuming and labor-

209 intensive. In this section, we introduce a way of automatically determining r_c and dis-
210 cuss how r_c influences the emission rate estimation (Figure S1).

211 First, we introduce a parameter ΔIME, which represents the additional mass en-
212 hancement as the radius expands a differential amount from r_{j-1} to r_j. Most of the in-
213 cremental mass enhancement is expected to be from the plume (ΔIME_p), while a small
214 amount may be from background noise (ΔIME_b). With a stable emission rate and wind
215 speed and direction, ΔIME_p would be a positive constant value as the radius expands
216 until the circle area reaches the plume boundary. Then ΔIME_p would drop to zero and
217 remain zero as radius further expands. On the other hand, ΔIME_b is proportional to
218 the ring area if the background noise pixels are randomly distributed. Thus, ΔIME_b would
219 linearly increase along the radius expansion. Consequently, the relationship between ΔIME
220 and r_j can be expressed as follows:

$$\Delta IME = \Delta IME_p + \Delta IME_b = \begin{cases} \Delta IME_p + \beta(2\pi\Delta r \cdot r_j - \pi\Delta r^2), & 0 < r_j \leq r_c \\ \beta(2\pi\Delta r \cdot r_j - \pi\Delta r^2), & r_j > r_c \end{cases} \quad (3)$$

222 where Δr is the incremental radius (pixel size) and β is the slope coefficient. In a
223 detectable and quantifiable emission event, ΔIME_b is expected to be much smaller than
224 ΔIME_p within the radius range $0-r_c$, so the minimum value of ΔIME would occur
225 at r_c due to the drop of ΔIME_p. Therefore, to automatically determine r_c, we calcu-
226 late ΔIME over a wide radius range and define r_c as the radius where the minimum ΔIME
227 is achieved. Note that ΔIME often exhibits fluctuations over small radius ranges. To
228 mitigate this effect, we set a starting radius r_s for the ΔIME calculation instead of be-
229 ginning at the plume origin. For the power plant dataset, we explore two scenarios with
230 r_s values of 100 m and 300 m. Further analysis is discussed in Section 3.1. For the LNG
231 terminal dataset, we set r_s as 100 m to ensure that only one plume is included within
232 the study area, considering the presence of multiple adjacent plumes in one terminal. Ad-
233 ditionally, an ending radius of r_c calculation is set as 1500 m to include even large CO_2
234 plumes with long plume lengths.

235 Based on equation 2 and 3, the relationship between Q and r_j can be further ex-
236 pressed as follows:

$$Q = \left(\frac{\overline{IME_p}}{r_j} + \frac{\overline{IME_b}}{r_j}\right)U_{10} = \begin{cases} U_{10}\left(\frac{\Delta IME_p}{\Delta r} + \frac{\beta\pi}{j}\sum_{k=1}^{j} r_k\right), & 0 < r_j \leq r_c \\ U_{10}\left(\frac{c}{j}\frac{\Delta IME_p}{\Delta r} + \frac{c}{j}\Delta IME_p\sum_{k=c+1}^{j}\frac{1}{r_k} + \frac{\beta\pi}{j}\sum_{k=1}^{j} r_k\right), & r_j > r_c \end{cases}$$
$$(4)$$

237 Therefore, the emission rate estimate would slightly increase within the radius range
238 $0 - r_c$, resulting in a modestly higher Q estimate at $r_j = r_c$ due to background noise
239 $(U_{10}\frac{\beta\pi}{j}\sum_{k=1}^{j} r_k)$. However, this bias from background noise can be ignored if ΔIME_b
240 is much smaller than ΔIME_p (see Section 3.1).

3 Results

3.1 Power Plant Emission Events

243 We compare the estimated emission rates to *in situ* CEMS measurements for the
244 47 power plant emission events. Two scenarios are considered, with the starting radius
245 during fetch radius calculation r_s of 300 m and 100 m, respectively. The uncertainty bounds
246 are generated by assuming ±25% errors of the mix ratio length minimum threshold α_l,
247 fetch radius r_c and wind speed U_{10}. We use ordinary least squares regression to assess
248 quantification accuracy (E. D. Sherwin et al., 2023; Rutherford et al., 2023). The sce-
249 nario with $r_s = 300$ m demonstrates the best performance (Figure 1). The estimates have

a robust correlation ($R^2 = 0.9149$) with the *in situ* data, with a tendency to somewhat underestimate emissions (slope = 0.8322) for emissions ranging from 200-3000 t/hr (metric tons per hour). The average estimate error is -2% (min/max interval [-64%, 127%]), with 81% of the estimates falling within ±50% of the *in situ* emission rates. However, if $r_s = 100$ m, there is a higher underestimation tendency (slope = 0.7371) in the range of 100-3000 t/hr, with $R^2 = 0.8445$ (Figure S2). These estimates have larger error (average -25%, [-83%, 41%]), but the proportion of estimates falling within ±50% of the *in situ* emission rates remains similar (79%).
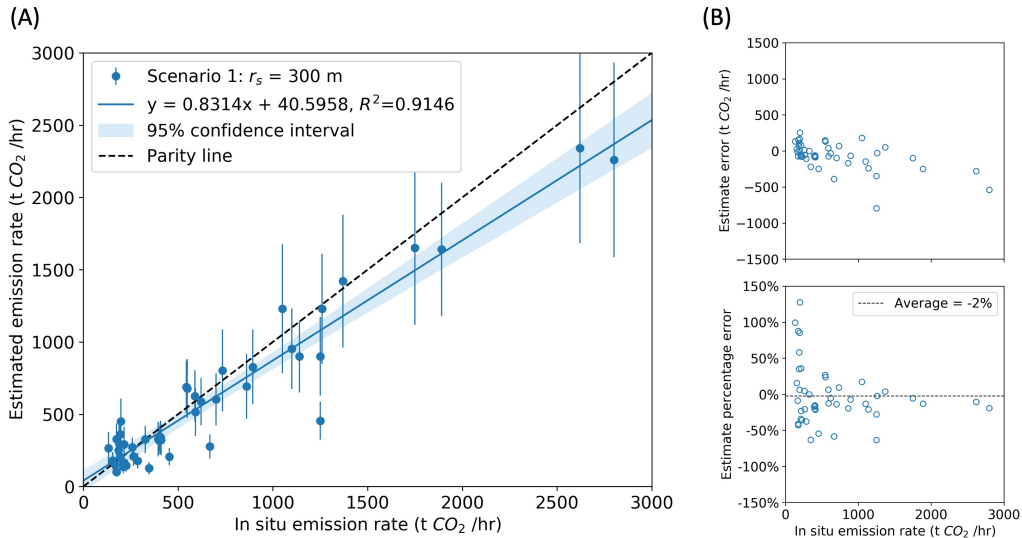
Figure 1. Power plant emission rate estimates compared to *in situ* emission rates in scenario 1: $r_s = 300$ m. (A): Emission rate estimates. (B): Emission rate estimation errors.

13 emission events in this study with *in situ* emission rate ranging in 150-1800 t/hr were also analyzed in Cusworth et al. (2021). They reported a lower R^2 (0.8840) compared to scenario 1 ($r_s = 300$ m) but higher than scenario 2 ($r_s = 100$ m). The average estimate error is 16% [-9%, 65%], with 85% of the estimates falling within ±50% of the *in situ* emission rates. The difference between the estimates in this study and Cusworth et al. (2021) is within ±60% for all the 13 events in both two scenarios (Figure S3).

Figure 2 shows a plume quantification example at the Four Corners Power Plant on August 4th, 2020 (see all plume results in Figure S5-S8 and Table S2). Based on the automatic fetch radius calculation, r_c is determined to be 563.5 m where the minimum ΔIME is achieved. The circular study area defined by r_c covers the whole plume, with few background noise pixels included. The emission rate is estimated as 1426 ± 459.76 t/hr, which is 104% ([71%, 138%]) of the *in situ* measured rate.

Note that our method includes as CO_2 signals all the pixels that meet the quantification criteria, without attempting to manually separate a masked plume. Therefore, it is possible that part of the resulting mass enhancement is from background noise instead of the plume. In Figure 2, for example, the pixels marked in red rectangles are very likely to be background noise. The IME of these pixels is around 4% of the IME in the study area, implying that the influence of background noise on the emission rate estimation is small. In another example in Figure S4 (B), however, the majority of the enhancement is likely to be background noise. The IME of these pixels accounts for around 60% of the IME in the study area. Some of these artifacts align with the surface features
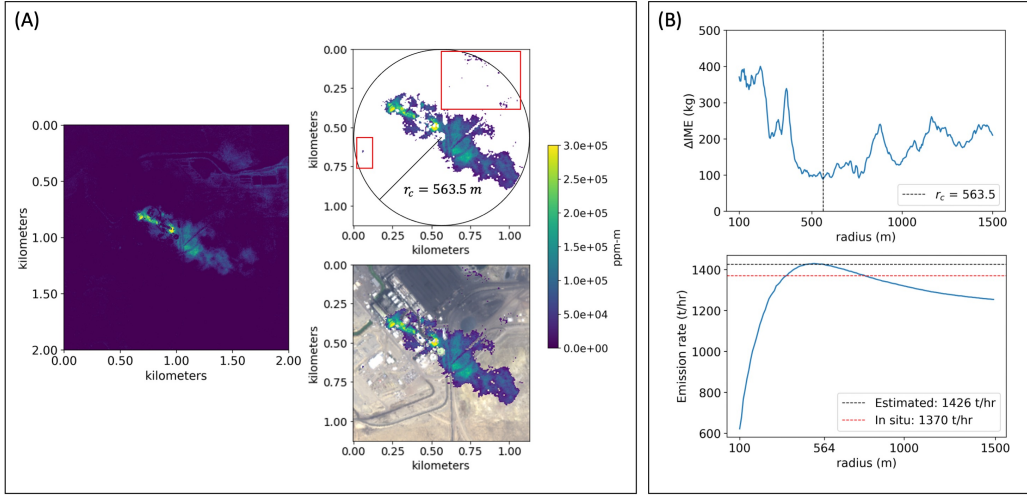
Figure 2. A power plant plume example. Time: 08/04/2020 17:07:56 UTC. Location: Four Corners Power Plant, (36.6862, -108.4775). (A) left: plume figure in a zoomed-out view (generated by the matched filter method); (A) right: plume figures in the circle study area of $r_c = 563.5$ m, with and without RGB basemap. Background noise is outlined by red rectangles. Note that both two starting radius ($r_s = 300$ m and $r_s = 100$ m) return the same r_c value in this example. (B) top: ΔIME over radius; (B) bottom: emission rate estimate Q as a function of radius r_c.

in shape, suggesting that the surface features are the true reason of spurious high CO_2 enhancement. Our emission rate estimate of this emission event is 1.85 times higher than *in situ* data, implying that background noise can lead to overestimation.

Removing background noise from CO_2 plumes remains difficult to implement systematically across a diverse set of observing environments. However, given these issues, the results from Figure 1 show that the approaches implemented in this study are sufficient to accurately quantify power plant CO_2 emissions. As methods to remove noise from retrievals are refined, we anticipate further improvement and agreement of remotely sensed emission estimates to ground truth.

3.2 LNG Terminal Emission Events

Compared to power plants, CO_2 plumes from LNG terminals exhibit several distinct characteristics. First, LNG terminal plumes are typically smaller in size and have lower emission rates. Second, the presence of complex background surface features in the vicinity of LNG terminal point sources introduces more background noise. Third, in large terminals with multiple independent LNG trains, there are often multiple plumes present. The first two aspects suggest that a smaller r_s (scenario 2) would be more suitable to mitigate overestimation by including less background noise. The last aspect suggests that it is more appropriate to treat multiple CO_2 plumes as individual emission events rather than a single event, so a smaller r_s (scenario 2) is also preferred. Therefore, our method with $r_s = 100m$ is used for LNG terminal CO_2 quantification.

In Sabine Pass, a total of 8 point sources are identified during 6 overpasses. Among these point sources, 5 are from fuel combustion and 3 are from flare combustion. The emission rate estimates of the fuel combustion point sources range from 219.69 ± 54.95 to 1083.22 ± 308.06 t/hr. Flare combustion point sources exhibit lower emissions rate

estimates, ranging from 247.75 ± 84.62 to 508.44 ± 137.29 t/hr. Point source B has the highest number of emission events, with emission rate estimates ranging from 269.59 ± 77.89 to 1022.65 ± 280.10 t/hr. There are two groups of flare combustion events on October 30th 2021, with a time difference of approximately 5 minutes between them. The plumes display similar lengths and shapes at both timestamps, and the emission rate estimates of the latter events are 13-39% higher than the former ones. In Cameron, 3 point sources from fuel combustion are identified during 2 overpasses. The emission rates range from 91.64 ± 25.81 to 265.61 ± 67.80 t/hr, suggesting that all three point sources have emission rates of similar magnitude (see plume examples in Figure 3 and all LNG plume results in Figure S9-S10 and Table S3).
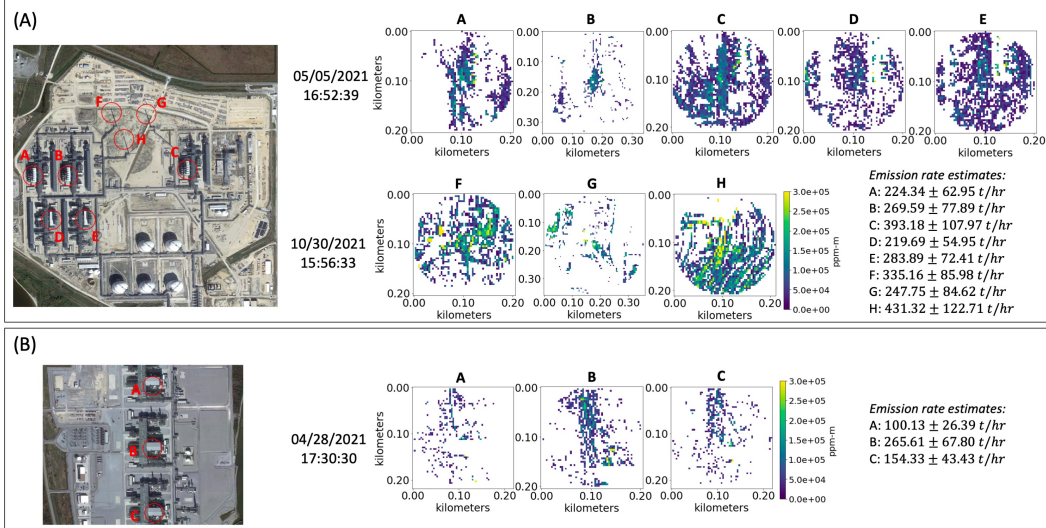

Figure 3. LNG plume examples. (A) Sabine Pass terminal. Point source A-E are from fuel combustion and point source F-H are from flare combustion. (B) Cameron terminal. Point source A-C are from fuel combustion.

Overall, the emission rate estimates of the LNG terminal plumes approximately range from 100-1000 t/hr. The interquartile range of LNG terminal plumes [220.85, 389.45] t/hr falls within the interquartile range of the power plant dataset [212.45, 877.74] t/hr (Figure S11), suggesting that our method has comparable capability in estimating CO_2 emissions for both LNG terminals and power plants. However, it is important to note that the LNG terminal plumes exhibit higher levels of background noise, which can introduce greater variance in our estimates compared to the power plants. Future work is needed to assess whether this is the case. It may be possible to increase the quantification accuracy by manually identifying emission plumes and excluding background noise before applying the current quantification method.

3.3 Life-cycle Carbon Intensity

In this section, we conduct a rough estimation of liquefaction CI based on our 22 emission rate samples, although a larger dataset would aid in generating a more robust estimation. First, we sum up the emission rates of all the point sources of each LNG terminal in each overpass. The total emission rates are considered as the daily average of each terminal, except for the date October 30th 2021, when we have two overpasses, so the average of these two is calculated. Then we obtain the daily export data of each LNG terminal from the U.S. Department of Energy (U.S. DOE, 2023), assuming that the amount

of exported LNG equals to the amount of liquefied LNG at the same day. There are cases where we fail to find records of LNG exports at the same day of the emission events, so the exports at the closest date after the emission event are used instead, assuming that LNG was officially recorded after being liquefied and transported. Finally, we calculate the CI of each date for each terminal and take the average (see Table S4).

Sabine Pass, with emissions data from 6 overpasses, has an average CI of 7.25 [2.45, 12.97] g CO_2 eq/MJ. Cameron has an average CI of 3.14 [2.91, 3.36] g CO_2 eq/MJ based on the emissions data of 2 overpasses. The numbers are mostly within the range of 2.4-8.8 g CO_2 eq/MJ in Abrahams et al. (2015), 4.1-7.7 g CO_2 eq/MJ in Balcombe et al. (2017) and 4.1-7.6 g CO_2 eq/MJ in Gan et al. (2020). Our estimate of Sabine Pass also aligns with the estimate of Roman-White et al. (2021), which is 4.64 g CO_2/MJ (100-year GWP) based on the 2018 GHGRP data of Sabine Pass. Note that the CO_2 emissions detected by this study are not the only sources of GHG emissions. Other sources include fugitive methane emissions and post-acid gas (AGR) CO_2 venting emissions, which require methane detection methods and a lower detection limit of our method to capture. However, fuel combustion accounts for over 98% of the total emissions (Roman-White et al., 2021), so we believe our method is still able to provide a whole picture of the liquefaction CI. Although in this estimation, the small amount of samples suggests that the temporal variability could be an important uncertainty source, we are confident that this method can greatly complement to a more robust estimation of the liquefaction life-cycle CI if with a larger dataset. When combined with methane detection, it can further contribute to a more efficient monitoring system of the carbon emissions along the LNG supply chain.

4 Conclusion

The rapid growth of U.S. LNG exports underscores the importance of CO_2 monitoring for LNG export terminals. However, existing inventories only provide annual/monthly emissions data reported by LNG operators for some major LNG terminals. This study presents a CO_2 emissions measuring method applied to LNG terminals using imaging spectroscopy data from AVIRIS-NG and GAO. The method is first validated using 47 power plant emission events with *in situ* measured data, then applied to 22 emission events in two major LNG terminals: Sabine Pass and Cameron. Results show that the emission rate estimates of the LNG terminal plumes approximately range from 100-1000 t/hr. At Sabine Pass, 8 point sources of either fuel combustion or flare combustion are identified, with emission rates ranging from 219.69 ± 54.95 to 1083.22 ± 308.06 t/hr. At Cameron, 3 point sources are identified with emission rates ranging from 91.64 ± 25.81 to 265.61 ± 67.80 t/hr. Based on these estimates, we calculate the life-cycle CI of two terminals as 7.25 [2.45, 12.97] g CO_2 eq/MJ and 3.14 [2.91, 3.36] g CO_2 eq/MJ, respectively.

We see a robust correlation between our emission rate estimates and *in situ* measured data of the power plant dataset, with the R^2 as 0.9146 and the average errors as -2% if the starting radius during fetch radius calculation r_s is set as 300 m. A smaller value of r_s is more suitable for small plumes with significant background noise, as it helps mitigate overestimation by including less background noise.

Compared to power plant CO_2 plumes, LNG terminal CO_2 plumes are generally smaller in shape, with lower emission rates and more background noise. This can introduce greater variance to our estimates compared to the power plant results, which we were only able to qualitatively assess in this study based on the number of available measurements at LNG facilities. However, the performance of our method on power plant emissions with similar magnitudes suggests comparable capabilities at LNG terminal CO_2 emissions quantification.

Our method provides an independent third-party data source with uniform measuring technology to the LNG terminal CO_2 emissions monitoring. Additionally, the emission measurements obtained by this method would help enable rapid responses to any unexpected increases in emissions. If with a larger emission dataset, our method is able to provide a more robust life-cycle CI estimation for the LNG liquefaction. When combined with methane detection, it can further contribute to a more efficient monitoring system of the GHG emissions along the LNG supply chain. Furthermore, this study validates the quantification performance of imaging spectroscopy on the plumes with emission rate of 100-3000 t/hr, implying its potential for broader application in CO_2 top-down detection.

Open Research Section

Data Availability Statement

The Next-Generation Airborne Visible/Infrared Imaging Spectrometer (AVIRIS-NG) L1 radiances are available online at the AVIRIS-NG Data Portal (`https://avirisng.jpl.nasa.gov/dataportal/`). The Global Airborne Observatory (GAO) radiance data can be made available by contacting the Center for Global Discovery and Conservation Science (`https://globalfutures.asu.edu/gdcs/global-airborne-observatory/`) via email GregAsner@asu.edu.

References

Abrahams, L. S., Samaras, C., Griffin, W. M., & Matthews, H. S. (2015). Life cycle greenhouse gas emissions from U.S. liquefied natural gas exports: Implications for end uses. *Environmental Science & Technology*, *49*(5), 3237-3245. https://doi.org/10.1021/es505617p

Alam, S., Flora, A., Isaad, H., Jain, P., Jaller-Makarewicz, A. M., Morrison, K., . . . Williams-Derry, C. (2023). *Global LNG Outlook 2023-27* (Tech. Rep.). Institute for Energy Economics and Financial Analysis. `https://ieefa.org/resources/global-lng-outlook-2023-27`.

Apple Inc. (2023). *Dark Sky API.* `https://darksky.net/dev`.

Asner, G. P., Knapp, D. E., Boardman, J., Green, R. O., Kennedy-Bowdoin, T., Eastwood, M., . . . Field, C. B. (2012). Carnegie Airborne Observatory-2: Increasing science data dimensionality via high-fidelity multi-sensor fusion. *Remote Sensing of Environment*, *124*, 454-465. https://doi.org/10.1016/j.rse.2012.06.012

Ayasse, A. K., Dennison, P. E., Foote, M., Thorpe, A. K., Joshi, S., Green, R. O., . . . Roberts, D. A. (2019). Methane mapping with future satellite imaging spectrometers. *Remote Sensing*, *11*(24). https://doi.org/10.3390/rs11243054

Ayasse, A. K., Thorpe, A. K., Roberts, D. A., Funk, C. C., Dennison, P. E., Frankenberg, C., . . . Aubrey, A. D. (2018). Evaluating the effects of surface properties on methane retrievals using a synthetic airborne visible/infrared

imaging spectrometer next generation (AVIRIS-NG) image. *Remote Sensing of Environment*, *215*, 386-397. https://doi.org/10.1016/j.rse.2018.06.018

Balcombe, P., Anderson, K., Speirs, J., Brandon, N., & Hawkes, A. (2017). The natural gas supply chain: The importance of methane and carbon dioxide emissions. *ACS Sustainable Chemistry & Engineering*, *5*(1), 3-20. https://doi.org/10.1021/acssuschemeng.6b00144

Barnett, P. J. (2010). *Life Cycle Assessment (LCA) of liquefied Natural Gas (LNG) and its environmental impact as a low carbon energy source* . University of Southern Queensland. (Available at https://sear.unisq.edu.au/18409/1/ Barnett_2010.pdf)

Chen, Y., Sherwin, E. D., Berman, E. S., Jones, B. B., Gordon, M. P., Wetherley, E. B., . . . Brandt, A. R. (2022). Quantifying regional methane emissions in the new mexico permian basin with a comprehensive aerial survey. *Environmental Science & Technology*, *56*(7), 4317–4323. https://doi.org/10.1021/ acs.est.1c06458

Cohen, A. K. (2013). *The shale gas paradox - assessing the impacts of the shale gas revolution on electricity markets and climate change* . Harvard College, Cambridge, MA. (Available at https://www.hks.harvard.edu/sites/default/ files/centers/mrcbg/files/cohen_awp_14x.pdf)

Cusworth, D. H., Duren, R. M., Thorpe, A. K., Eastwood, M. L., Green, R. O., Dennison, P. E., . . . Miller, C. E. (2021). Quantifying global power plant carbon dioxide emissions with imaging spectroscopy. *AGU Advances*, *2*(2), e2020AV000350. https://doi.org/10.1029/2020AV000350

Dennison, P. E., Thorpe, A. K., Pardyjak, E. R., Roberts, D. A., Qi, Y., Green, R. O., . . . Funk, C. C. (2013). High spatial resolution mapping of elevated atmospheric carbon dioxide using airborne imaging spectroscopy: Radiative transfer modeling and power plant plume detection. *Remote Sensing of Environment*, *139*, 116-129. https://doi.org/10.1016/j.rse.2013.08.001

Duren, R. M., Thorpe, A. K., Foster, K. T., Rafiq, T., Hopkins, F. M., Yadav, V., . . . others (2019). California's methane super-emitters. *Nature*, *575*(7781), 180–184. https://doi.org/10.1038/s41586-019-1720-3

Foote, M. D., Dennison, P. E., Sullivan, P. R., O'Neill, K. B., Thorpe, A. K., Thompson, D. R., . . . Joshi, S. C. (2021). Impact of scene-specific enhancement spectra on matched filter greenhouse gas retrievals from imaging spectroscopy. *Remote Sensing of Environment*, *264*, 112574. https://doi.org/ 10.1016/j.rse.2021.112574

Frankenberg, C., Thorpe, A. K., Thompson, D. R., Hulley, G., Kort, E. A., Vance, N., . . . Green, R. O. (2016). Airborne methane remote measurements reveal heavy-tail flux distribution in Four Corners region. *Proceedings of the National Academy of Sciences*, *113*(35), 9734-9739. https://doi.org/10.1073/ pnas.1605617113

Friedlingstein, P., O'Sullivan, M., Jones, M. W., Andrew, R. M., Gregor, L., Hauck, J., . . . Zheng, B. (2022). Global Carbon Budget 2022. *Earth System Science Data*, *14*(11), 4811–4900. https://doi.org/10.5194/essd-12-3269-2020

Gan, Y., El-Houjeiri, H. M., Badahdah, A., Lu, Z., Cai, H., Przesmitzki, S., & Wang, M. (2020). Carbon footprint of global natural gas supplies to China. *Nature Communications*, *11*(1), 824. https://doi.org/10.1038/ s41467-020-14606-4

Hamedi, M., Farahani, R. Z., Husseini, M. M., & Esmaeilian, G. R. (2009). A distribution planning model for natural gas supply chain: A case study. *Energy Policy*, *37*(3), 799-812. https://doi.org/10.1016/j.enpol.2008.10.030

Okamura, T., Furukawa, M., & Ishitani, H. (2007). Future forecast for life-cycle greenhouse gas emissions of lng and city gas 13a. *Applied Energy*, *84*(11), 1136-1149. https://doi.org/10.1016/j.apenergy.2007.05.005

Roman-White, S. A., Littlefield, J. A., Fleury, K. G., Allen, D. T., Balcombe, P.,

Konschnik, K. E., . . . George, F. (2021). LNG supply chains: A supplier-specific life-cycle assessment for improved emission accounting. *ACS Sustainable Chemistry & Engineering*, *9*(32), 10857–10867. https://doi.org/10.1021/acssuschemeng.1c03307

Rutherford, J. S., Sherwin, E. D., Chen, Y., Aminfard, S., & Brandt, A. R. (2023). Evaluating methane emission quantification performance and uncertainty of aerial technologies via high-volume single-blind controlled releases. https://doi.org/10.31223/X5KQ0X

Sherwin, E., Rutherford, J., Zhang, Z., Chen, Y., Wetherley, E., Yakovlev, P., . . . others (2023). Quantifying oil and natural gas system emissions using one million aerial site measurements. (preprint on Research Square at `https://doi.org/10.21203/rs.3.rs-2406848/v1`)

Sherwin, E. D., Rutherford, J. S., Chen, Y., Aminfard, S., Kort, E. A., Jackson, R. B., & Brandt, A. R. (2023). Single-blind validation of space-based point-source detection and quantification of onshore methane emissions. *Scientific Reports*, *13*(1), 3836. https://doi.org/10.1038/s41598-023-30761-2

Thorpe, A. K., Frankenberg, C., Aubrey, A. D., Roberts, D. A., Nottrott, A. A., Rahn, T. A., . . . McFadden, J. P. (2016). Mapping methane concentrations from a controlled release experiment using the next generation airborne visible/infrared imaging spectrometer (AVIRIS-NG). *Remote Sensing of Environment*, *179*, 104-115. https://doi.org/10.1016/j.rse.2016.03.032

Thorpe, A. K., Frankenberg, C., Thompson, D. R., Duren, R. M., Aubrey, A. D., Bue, B. D., . . . Dennison, P. E. (2017). Airborne DOAS retrievals of methane, carbon dioxide, and water vapor concentrations at high spatial resolution: application to AVIRIS-NG. *Atmospheric Measurement Techniques*, *10*(10), 3833–3850. https://doi.org/10.5194/amt-10-3833-2017

U.S. DOE. (2023). *LNG Reports.* `https://www.energy.gov/fecm/listings/lng-reports`.

U.S. EIA. (2022). *U.S. LNG export capacity to grow as three additional projects begin construction.* `https://www.eia.gov/todayinenergy/detail.php?id=53719`.

U.S. EIA. (2023). *Europe was the main destination for U.S. LNG exports in 2022.* `https://www.eia.gov/todayinenergy/detail.php?id=55920`.

U.S. EPA. (2022). *Facility Level Information on Greenhouse gases Tool (FLIGHT).* `https://ghgdata.epa.gov/ghgp`.

U.S. EPA. (2023). *Clean Air Markets Program Data (CAMPD).* `https://campd.epa.gov`.

Zarei, J., & Amin-Naseri, M. R. (2019). An integrated optimization model for natural gas supply chain. *Energy*, *185*, 1114-1130. https://doi.org/10.1016/j.energy.2019.07.117